Title

Coherent Electronic Band Structure of TiTe2/TiSe2 Moiré Bilayer



Journal

ACS Nano, 15(2)

ISSN

1936-0851

Authors

Lin, Meng-Kai

He, Tao

Hlevyack, Joseph A

et al.

Publication Date

2021-02-23

DOI

10.1021/acsnano.0c10352

Peer reviewed

# Coherent Electronic Band Structure of $TiTe_2/TiSe_2$ Moiré Bilayer

Meng-Kai Lin,[†,‡,◇] Tao He,[#,◇] Joseph A. Hlevyack,[†,‡] Peng Chen,[‖] Sung-Kwan Mo,[⊥] Mei-Yin Chou,[#,§,*] and T.-C. Chiang[†,‡,*]

[†]*Department of Physics, University of Illinois at Urbana-Champaign, Urbana, Illinois 61801, USA*

[‡]*Frederick Seitz Materials Research Laboratory, University of Illinois at Urbana-Champaign, Urbana, Illinois 61801, USA*

[#]*Institute of Atomic and Molecular Sciences, Academia Sinica, Taipei 10617, Taiwan*

[‖]*Key Laboratory of Artificial Structures and Quantum Control (Ministry of Education), Shenyang National Laboratory for Materials Science, and Shanghai Center for Complex Physics, School of Physics and Astronomy, Shanghai Jiao Tong University, Shanghai 200240, China*

[⊥]*Advanced Light Source, Lawrence Berkeley National Laboratory, Berkeley, California 94720, USA*

[§]*Department of Physics, National Taiwan University, Taipei 10617, Taiwan*

**Corresponding authors.**

[*]T.-C. Chiang, Email: tcchiang@illinois.edu

[*]Mei-Yin Chou, Email: mychou6@gate.sinica.edu.tw

**Additional author note.**

[◇]Equal contribution

## ABSTRACT

A van der Waals-bonded moiré bilayer formed by sequential growth of $TiSe_2$ and $TiTe_2$ monolayers exhibits emergent electronic structure as evidenced by angle-resolved photoemission band mapping. The two monolayers adopt the same lattice orientation but incommensurate lattice constants. Despite the lack of translational symmetry, sharp dispersive bands are observed. The dispersion relations appear distinct from those for the component monolayers alone. Theoretical calculations illustrate the formation of composite bands by coherent electronic coupling despite the weak interlayer bonding, which leads to band renormalization and energy shifts.

**KEYWORDS:** transition metal dichalcogenides, moiré bilayer, ultrathin film, heterostructure, emergent band structure

**TOC Graphic:**

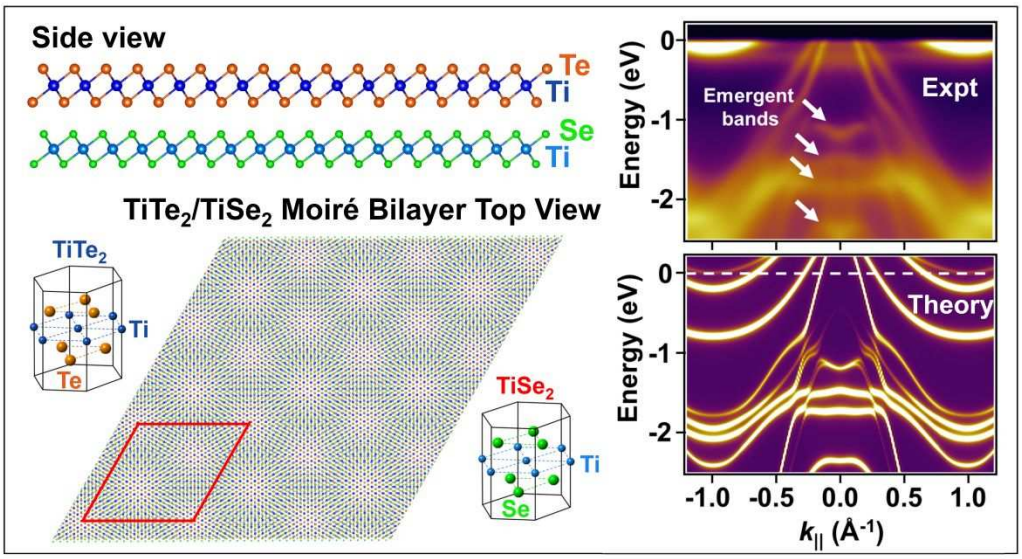

Two-dimensional moiré systems have attracted much interest due to their tunable properties, including superconductivity,[1-3] magnetic ordering,[4,5] and optical responses,[6,7] which can be exploited for nanoscale device applications. Such moiré systems can be fabricated by van der Waals bonding of two monolayers with a twist angle and/or with different lattice constants.[1-12] The vast choices of van der Waals monolayers available for bilayer assembly, including graphene,[1-3] boron nitride,[8-10] and the numerous transition metal dichalcogenides, make moiré bilayers a rich playground for emergent effects.[11-24] A key question is how to describe and model the electronic structure of such systems. Since translational symmetry is broken, Bloch's theorem, the basis for band structure formalism and a fundamental pillar for solid state physics, does not apply. A large approximately commensurate periodic moiré superlattice may be constructed in certain cases, but the moiré unit cell is generally very large. This is indeed the case for the bilayer system $TiTe_2/TiSe_2$ discussed in the present work. The in-plane lattice constants, $a_T$ = 3.777 and $a_S$ = 3.536 Å for $TiTe_2$ and $TiSe_2$, respectively,[13-15, 25] allow a near match with a moiré superlattice period of $15a_T$ ; $16a_S$ at a zero twist angle. The number of atoms in this approximate superlattice unit cell is 1443, too large for first-principles treatment including full atomic relaxation. The tiny Brillouin zone of the moiré superlattice would suggest essentially flat folded band dispersion relations.

To date, many monolayer systems prepared on incommensurate substrates (such as graphene or bilayer graphene) by van der Waals bonding have been examined by angle-resolved photoemission spectroscopy (ARPES).[13-18, 20-22] These moiré monolayers typically show a well-defined band structure very similar to that predicted or expected for an essentially freestanding monolayer with little influence from the substrate.[13-22] Evidently, incommensurate coupling across the van der Waals interface in such systems does not affect much the electronic structure of the

supported monolayer. The gradual slippage of lattice registry over the moiré superlattice unit cell gives rise to variations in local coupling, which may be effectively averaged out. By extrapolation, a moiré bilayer might be expected to be closely described by an incoherent superposition of the band structures from the two component monolayers. However, our ARPES results reported herein show that this is not true for the $TiTe_2/TiSe_2$ bilayer created by growing a $TiSe_2$ monolayer first on a bilayer-graphene-terminated 6*H*-SiC(0001) substrate followed by a $TiTe_2$ monolayer on top. The observed band dispersion relations are quite distinct from the band dispersions of $TiTe_2$ and $TiSe_2$ alone on the same substrate. An approximate but effective theoretical evaluation of the coherent composite band structure provides a framework to understand the electronic structure in such artificial systems.

## RESULTS AND DISCUSSION

**Atomic Structure of $TiTe_2/TiSe_2$ Moiré Bilayer.** Figure 1a shows the 1*T* trigonal unit cell structures of $TiTe_2$ and $TiSe_2$ and a top view of the $TiTe_2/TiSe_2$ bilayer structure, where a moiré modulation with a period of 56.6 Å is evident, as indicated by the rhombic superlattice unit cell. The residual mismatch is at the ~0.1% level. The regions marked by red, blue, and maroon circles are locations near AA, AB, and AB' stacking configurations, where A, B, and B' represent the in-plane site positions of the Ti atoms, the bottom Se/Te atoms, and the top Se/Te atoms in the unit cells, respectively. Detailed side and top views of the three stacking configurations are shown in Figure 1b. Figure 1c offers a visual comparison of the Brillouin zone sizes for $TiTe_2$, $TiSe_2$, and the moiré superlattice; the one for the moiré superlattice is amplified ten times for easy viewing.

**Structure Characterization of $TiSe_2$ Monolayer and $TiTe_2/TiSe_2$ Moiré Bilayer.** Experimentally, the $TiTe_2$ and $TiSe_2$ lattices in the bilayer are oriented in parallel epitaxy as evidenced by reflection high energy electron diffraction (RHEED) determination of the

crystallographic orientation and ARPES observation of the conduction band minimum at the $\overline{M}$ point. Figures 2a-c show RHEED patterns taken from a bilayer-graphene-terminated 6*H*-SiC(0001), the same after the growth of a $TiSe_2$ monolayer, and the same after further growth of a $TiTe_2$ monolayer, respectively. Line profiles for these RHEED patterns in Figure 2d show first-order diffraction peaks along the $\overline{\Gamma M}$ direction on the two sides of the central peak. As seen in Figure 2d, after the growth of $TiSe_2$ monolayer, the first-order peaks of bilayer graphene vanish, and two new peaks with narrower spatial separation show up, which correspond to the $TiSe_2$ monolayer lattice with a lattice constant of 3.54 Å. The results indicate that the surface of bilayer graphene is now fully covered by a $TiSe_2$ overlayer. By adding a $TiTe_2$ monolayer on top of the $TiSe_2$ monolayer, the first-order peaks are closer together for the $TiTe_2/TiSe_2$ bilayer than for the $TiSe_2$ monolayer alone due to the larger lattice constant of $TiTe_2$. Furthermore, the bilayer peaks are somewhat broader (amplified views in Figure 2e) and can be well-represented by two components with an intensity ratio of 0.28 from the fitting. The stronger and weaker components can be assigned to the $TiTe_2$ top layer and the $TiSe_2$ bottom layer, respectively, with the peaks at the expected positions based on the lattice constants. The intensity ratio is consistent with the very short probing depth of the RHEED beam (~5 Å).

**ARPES Spectra and Electronic Band Structure.** Figure 3a shows mirror symmetrized ARPES maps along the $\overline{M} - \bar{\Gamma} - \overline{M}$ direction acquired with 58-eV photons at 300 K from monolayer $TiSe_2$, moiré bilayer $TiTe_2/TiSe_2$, and monolayer $TiTe_2$. The corresponding second-derivative maps are presented in Figure 3b. Similar data taken at a lower temperature of 20 K and the corresponding second-derivative maps are displayed in Figures 3c and d, respectively. Theoretical band dispersion relations for monolayer $TiSe_2$ and monolayer $TiTe_2$ are included in the left and right panels in Figure 3b and d as blue and red curves, respectively, for comparison with the monolayer

data; the blue and red curves are both included for the central panels for comparison with the moiré bilayer data. The ARPES results for the two monolayers are consistent with prior studies.[13,14] For the $TiSe_2$ monolayer at 300 K (Figures 3a and b), the main features consist of a small part just below the Fermi level of a convex Ti 3*d* conduction band centered about $\overline{M}$, two spin-orbit-split convex Se 4*p* valence bands centered about the $\overline{\Gamma}$ point with their apexes reaching near the Fermi level, and another valence band at lower energies that form a hybridization gap with the upper valence bands. For the $TiTe_2$ monolayer at 300 K, the band features are similar, but the valence bands are shifted to higher energies with more of them now visible at lower energies. The top portions of the Te 5*p* bands reach above the Fermi level. The considerable indirect overlap in energy of the Te 5*p* and Ti 3*d* states makes the $TiTe_2$ monolayer a semimetal. At lower energies (below -1 eV) and near the zone center, three valence bands with complex shapes and gap structures are evident, instead of just one band within the same energy range for $TiSe_2$. The ARPES data taken at 20 K (Figures 3c and d) look very similar, but the bands appear sharper and more distinct because of reduced thermal broadening and a lower thermal diffuse background at this temperature. A slight complication is that the ARPES maps for the $TiSe_2$ and $TiTe_2$ monolayers (Figures 3c and d) now contain additional features from folded bands arising from a (2x2) charge density wave (CDW) transition at 232 and 92 K, respectively.[13,14] The $TiTe_2/TiSe_2$ bilayer does not show such band folding, indicative of the absence of a (2x2) CDW. The absence of the CDW in $TiTe_2/TiSe_2$ bilayer can be attributed to the interlayer van der Waals coupling; similar suppression of the CDW from interfacial coupling has been observed for single layer $TiTe_2$ monolayers grown on different substrates.[23]

The monolayer ARPES band maps at 20 K, other than the CDW features, are in good agreement with the corresponding theoretical results (Figures 3c and d). For the $TiTe_2/TiSe_2$

bilayer, the measured band dispersions superficially resemble the monolayer cases despite the lack of translational symmetry and a very large moiré unit cell (or a very small moiré Brillouin zone). However, the superimposed band dispersion relations of monolayer $TiTe_2$ and monolayer $TiSe_2$ (central panels of Figures 3b and d) do not describe the bilayer data in detail. A major emergent feature, clearly distinct from the individual monolayer cases, is the band marked C1 in Figure 3. This composite band specific to the bilayer also exhibits roughly a double-hump shape but is located at substantially higher energies (closer to the Fermi level) than the $TiTe_2$ and $TiSe_2$ cases. Furthermore, this band shows a gap near the outer edge of each hump. The emergence of this dispersive composite band with a complex shape and at a substantially higher energy is evidence for coherent coupling between the two monolayers. If the bilayer were made of two incoherent monolayers, we would expect only a mixture of the component bands. The strong dispersion suggests that the system can still be described in terms of a band structure. Additional composite bands C2-C4 are indicated in Figure 3. Again, these cannot be described in terms of a combination or mixture of the bands from the individual monolayers.

**Theoretical Approach and Comparison of Band Structure.** Theoretical simulations of the composite-band effects are complicated by the large moiré unit cell, even with the residual mismatch ignored. It is not feasible to perform first-principles calculations where local atomic relaxation can be expected. Instead, we adopt the following approximations. Three major local stacking patterns, AA, AB, and AB', are considered (Figure 1b) with the $TiTe_2$ and $TiSe_2$ lattices constrained to the same average in-plane lattice constant. The vertical van der Waals bonding distance is optimized separately for each stacking configuration, with the resulting vertical layer spacing $c$ given in Figure 1b. The value of $c$ is the smallest for AA stacking, which can be related to the fact that both $TiTe_2$ and $TiSe_2$ by themselves crystalize in the 1*T* polymorph with the AA

stacking configuration, and it is very close to the average *c* value for bulk $TiTe_2$ and $TiSe_2$ as expected (Figure 1). Forcing the layer registry to AB or AB' leads to an energetically unfavorable configuration, which would cause the layers to move apart. The AB stacking puts the bottom Te atoms of the $TiTe_2$ monolayer directly on top of the top Se atoms of the $TiSe_2$ monolayer, instead of hollow sites. This geometry is expected to be least favorable, and indeed, the computed *c* value is the largest. The band structure for each configuration is then computed using the GGA + *U* method, with the *U* parameter chosen to be the average of those for $TiSe_2$ and $TiTe_2$. Separate calculations for $TiSe_2$ and $TiTe_2$ reveal that the change in the *U* parameter for each case results in only minor modifications to the respective band structures (see the Supporting Information). The average band structure for the three configurations is then taken to be a good representation for the composite bilayer system.

The calculated composite band structure, shown in Figure 4a, is color-coded with the orange (green) color indicating the weight from the top $TiTe_2$ (bottom $TiSe_2$) monolayer. Hybridization effects for the bands are quite evident. ARPES, with an effective probing depth of just ~5 Å, should reveal mostly bands with a strong weight in the top $TiTe_2$ layer. The same computed band structure plotted with an intensity scale indicating the surface-monolayer weight is shown in Figure 4b, which should mimic the ARPES data, provided that variations in ARPES matrix elements for the different bands are ignored. The ARPES data at 20 K and its second derivative are reproduced in Figures 4c and d, respectively, for side-by-side comparisons, but the intensity scale for a portion of Figure 4d has been adjusted to highlight the composite bands C1-C4. Included in Figure 4c are the theoretical bands (white dots) plotted over one half of the ARPES map; the size of each white dot is proportional to the calculated weight from the top $TiTe_2$ layer for an indication of the expected ARPES intensity variation. Evidently, the composite bands C1-

C4 are well-reproduced by the calculation. In particular, band C1 with its double humps and a hybridization gap on the outer edge of each hump is well-reproduced both in terms of its shape and energy position. Bands C2-C4, with their complex shapes near the zone center, are also well-reproduced. Once again, these composite bands cannot be described in terms of a combination or mixture of the bands from the component monolayers. The bands become less distinct away from the zone center, but the agreement remains generally good. However, an electron band centered near the zone boundary with its bottom at about -0.8 eV is largely missing in the experiment, which may be caused by a very weak photoemission matrix element.

Each stacking configuration, if extended to infinity, is expected to exhibit a different band structure. However, the differences in band structure among the three different stacking configurations are relatively minor because of the weakness of the interlayer van der Waals bonding (see Figure S3 in the Supporting Information), and the local electronic states for the moiré structure are expected to follow adiabatically the stacking variations over the different parts of the unit cell. Coherent coupling of the wave functions over the different parts gives rise to a single band structure with sharp (emergent) superlattice bands that are distinct from a statistical mixture. Our results are a direct demonstration of the coherent nature of the electronic structure. The averaging of the band energies for the different stacking configurations follows from the usual first-order calculations of the expectation values for the energy, which is appropriate for a superlattice with a weak modulation. Specifically, the energy for the *i*-th band for the bilayer is given by

$$E_i(\mathbf{k}) = \langle \psi_i(\mathbf{k}) | H | \psi_i(\mathbf{k}) \rangle \qquad (1)$$

where $H$ is the Hamiltonian. The wave function $\psi_i(\mathbf{k})$ various adiabatically over the moiré unit cell and adopts the form $\psi_i^S(\mathbf{k})$ locally over each stacking configuration $S$. To first order,

$$E_i(\mathbf{k}) = \frac{1}{N}\sum_S \left\langle \psi_i^S(\mathbf{k}) \middle| H \middle| \psi_i^S(\mathbf{k}) \right\rangle = \frac{1}{N}\sum_S E_i^S(\mathbf{k}) \qquad (2)$$

where $1/N$ is the fractional area for each stacking configuration $S$ within the moiré unit cell. Equation (2) is employed in our theoretical construction of the average band structure from the three major stacking configurations.

## CONCLUSIONS

Two major conclusions can be drawn. First, moiré bilayers, such as $TiTe_2/TiSe_2$ considered here, can exhibit an emergent or modified band structure arising from the coherent coupling of component monolayers, despite the lack of translational symmetry. This is likely the underlying mechanism for the reported tunable properties in such systems, including superconductivity, magnetism, and optical responses. Since the band structure of a solid generally determines all of its properties, a modified band structure by layer stacking is a promising way to create unusual or useful properties. The $TiTe_2/TiSe_2$ bilayer band structure measured by ARPES is sharp, which enables a theoretical analysis. Second, theoretical simulations for moiré bilayers, known to be difficult due to the lack of translational symmetry or a very large (approximate) unit cell, can be done effectively by keeping just the essential ingredients, as illustrated here for the composite band structure of the $TiTe_2/TiSe_2$ moiré bilayer. A successful demonstration in the present case suggests that the methodology may be applicable to other cases.

## METHODS

### Sample preparation

6*H*-SiC(0001) substrates were prepared by multiple cycles of high-temperature annealing, which cleans the surface and removes Si to leave the substrate's surface terminated by bilayer graphene. $TiSe_2$ was grown at a rate of one monolayer per 30 minutes by co-deposition of Ti and Se from an electron-beam evaporator and an effusion cell, respectively, under a high Se overpressure and with the substrate maintained at 250 ˚C.[14,15] Afterwards, a single layer of $TiTe_2$ was grown on top of the $TiSe_2$ film in a similar manner but with the substrate maintained at 280 ˚C.[13,23] ARPES measurements were performed using 58-eV photons and a Scienta R4000 analyzer at Beamline 10.0.1.1, Advanced Light Source. The monolayer coverages for the $TiSe_2$ and $TiTe_2$ film growths are based on absolute film thickness calibration as demonstrated in prior studies.[13,15] As the film thickness increases through the sequence of 0, 1, 2, … layers during the film growth, discrete changes in ARPES arising from band splitting are readily observed. This discrete evolution of quantum well states, sensitive to the film thickness, provides the absolute thickness calibration.

### Computational details

First-principles calculations were performed in the framework of density functional theory (DFT) using the projector augmented wave (PAW) method within the Vienna *ab Initio* Simulation Package (VASP).[26-28] The GGA and the PBE exchange-correlation functionals were employed to calculate the electronic structure.[29] A cutoff energy of 320 eV and a 18×18×1 *k*-space mesh were employed. Periodic slabs with a vacuum gap larger than 26 Å were adopted for the monolayer and bilayer configurations, with dipole correction included for the latter. The convergence criterion for the ground-state total energy was $10^{-6}$ eV, and atomic relaxation continued until the atomic forces

were less than $10^{-3}$ eV/Å. Interlayer spacing was optimized with the van der Waals correction based on the optB86b-vdW functional for the $TiTe_2/TiSe_2$ bilayer.[30,31] For a more accurate determination of the energy levels in the presence of interlayer interaction, the Ti $3s^2$ and $3p^6$ orbitals were treated as valence states. Hubbard $U$ corrections for the Ti $3d$ states were implemented for computing the total energy, energy bands, and charge density. The Hubbard parameter was found to be $U$ = 5.2 and 3.2 eV for $TiSe_2$ and $TiTe_2$, respectively, based on fits to the band structures determined by the HSE06 hybrid functional. For the bilayer system, the in-plane lattice constant $a$ and the $U$ parameter were set to the average value of those for $TiTe_2$ and $TiSe_2$. A twofold denser $k$-mesh was used to determine the Fermi level. The spin-orbit interaction was included in the calculations.

## ASSOCIATED CONTENT

### Supporting Information

1. Choice of $U$ in GGA + $U$ calculations for the $TiTe_2/TiSe_2$ bilayer.

2. Comparison of band structures for the AA, AB, and AB' stacking configurations with the average band structure.

## ACKNOWEDGLMENTS

This work is supported by the U.S. Department of Energy (DOE), Office of Science, Office of Basic Energy Sciences, Division of Materials Science and Engineering, under Grant No. DE-FG02-07ER46383 (T.C.C.). This research utilized resources of the Advanced Light Source, which is a DOE Office of Science User Facility under contract No. DE-AC02-05CH11231. T.H. and M.Y.C. acknowledge the support from Academia Sinica, Taiwan.

## REFERENCES

(1) Balents, L.; Dean, C. R.; Efetov, D. K.; Young, A. F. Superconductivity and Strong Correlations in Moiré Flat Bands. *Nat. Phys.* **2020**, 16, 725.

(2) Chen, G.; Sharpe, A. L.; Gallagher, P.; Rosen, I. T.; Fox, E. J.; Jiang, L.; Lyu, B.; Li, H.; Watanabe, K.; Taniguchi, T.; Jung, J.; Shi, Z.; Goldhaber-Gordon, D.; Zhang, Y.; Wang, F. Signatures of Tunable Superconductivity in a Trilayer Graphene Moiré Superlattice. *Nature* **2019**, 572, 215.

(3) Cao, Y.; Fatemi, V.; Fang, S.; Watanabe, K.; Taniguchi, T.; Kaxiras, E.; Jarillo-Herrero, P. Unconventional Superconductivity in Magic-Angle Graphene Superlattices. *Nature* **2018**, 556, 43.

(4) Hejazi, K.; Luo, Z. X.; Balents, L. Noncollinear Phases in Moiré Magnets. PNAS **2020**, 117, 10721.

(5) Kiese, D.; Buessen, F. L.; Hickey, C.; Trebst, S.; Scherer, M. M. Emergence and Stability of Spin-Valley Entangled Quantum Liquids in Moiré Heterostructures. *Phys. Rev. Res.* **2020**, 2, 013370.

(6) Tran, K.; Moody, G.; Wu, F.; Lu, X.; Choi, J.; Kim, K.; Rai, A.; Sanchez, D. A.; Quan, J.; Singh, A.; Embley, J.; Zepeda, A.; Campbell, M.; Autry, T.; Taniguchi, T.; Watanabe, K.; Lu, N.; Banerjee, S. K.; Silverman, K. L.; Kim, Suenne, Tutuc, E.; *et al.* Evidence for Moiré Excitons in van der Waals Heterostructures. *Nature* **2019**, 567, 71.

(7) Zhang, N.; Surrente, A.; Baranowski, M.; Maude, D. K.; Gant, P.; Castellanos-Gomez, A.; Plochocka, P. Moiré Intralayer Excitons in a $MoSe_2/MoS_2$ Heterostructure. *Nano Lett.* **2018**, 18, 7651.

(8) Finney, N. R.; Yankowitz, M.; Muraleetharan, L.; Watanabe, K.; Taniguchi, T.; Dean, C. R.; Hone, J. Tunable Crystal Symmetry in Graphene-Boron Nitride Heterostructures with Coexisting Moiré Superlattices. *Nat. Nanotechnol.* **2019**, 14, 1029.

(9) Neek-Amal, M.; Peeters, F. M. Graphene on Boron-Nitride: Moiré Pattern in the van der Waals Energy. *Appl. Phys. Lett.* **2014**, 104, 041909.

(10) Summerfield, A.; Kozikov, A.; Cheng, T. S.; Davies, A.; Cho, Y. J.; Khlobystov, A. N.; Mellor, C. J.; Foxon, C. T.; Watanabe, K.; Taniguchi, T.; Eaves, L.; Novoselov, K. S.; Novikov, S. V.; Beton, P. H. Moiré-Modulated Conductance of Hexagonal Boron Nitride Tunnel Barriers. *Nano Lett.* **2018**, 18, 4241.

(11) Rosenberger, M. R.; Chuang, H. J.; Phillips, M.; Oleshko, V. P.; McCreary, K. M.; Sivaram, S. V.; Hellberg, C. S.; Jonker, B. T. Twist Angle-Dependent Atomic Reconstruction and Moiré Patterns in Transition Metal Dichalcogenide Heterostructures. *ACS Nano* **2020**, 14, 4550.

(12) Zhang, Z.; Wang, Y.; Watanabe, K.; Taniguchi, T.; Ueno, K.; Tutuc, E.; LeRoy, B. J. Flat Bands in Twisted Bilayer Transition Metal Dichalcogenides. *Nat. Phys.* **2020**, 16, 1093.

(13) Chen, P.; Pai, W. W.; Chan, Y. -H.; Takayama, A.; Xu, C. -Z.; Karn, A.; Hasegawa, S.; Chou, M. Y.; Mo, S. -K.; Fedorov, A. -V.; Chiang, T. -C. Emergence of Charge Density Waves and a Pseudogap in Single-Layer $TiTe_2$. *Nat. Commun.* **2017**, 8, 516.

(14) Chen, P.; Chan, Y. -H.; Fang, X. -Y.; Zhang, Y.; Chou, M. Y.; Mo, S. -K.; Hussain, Z.; Fedorov, A. -V.; Chiang, T. -C. Charge Density Wave Transition in Single-Layer Titanium Diselenide. *Nat. Commun.* **2015**, 6, 8943.

(15) Chen, P.; Chan, Y. -H.; Wong, M. -H.; Fang, X. -Y.; Chou, M. Y.; Mo, S. -K.; Hussian, Z.; Fedorov, A. -V.; Chiang, T. -C. Dimensional Effects on the Charge Density Waves in Ultrathin Films of $TiSe_2$. *Nano Lett.* **2016**, 16, 6331.

(16) Chen, P.; Pai, W. W.; Chan, Y. -H.; Madhavan, V.; Chou, M. Y.; Mo, S. -K.; Fedorov, A. -V.; Chiang, T. -C. Unique Gap Structure and Symmetry of the Charge Density Wave in Single-Layer $VSe_2$. *Phy. Rev. Lett.* **2018**, 121, 196402.

(17) Lin, M. K., Villaos, R. A. B.; Hlevyack, J. A.; Chen, P.; Liu, R. Y.; Hsu, C. H.; Avila, J.; Mo, S. -K.; Chuang, F. C.; Chiang, T. -C. Dimensionality-Mediated Semimetal-Semiconductor Transition in Ultrathin $PtTe_2$ films. *Phys. Rev. Letts.* **2020**, 124, 036402.

(18) Ugeda, M. M.; Bradley, A. J.; Zhang, Y.; Onishi, S.; Chen, Y.; Ruan, W.; Ojeda-Aristizabal, C.; Ryu, H.; Edmonds, M. T.; Tsai, H. Z.; Riss, A.; Mo, S. -K.; Lee, D.; Zettl, A.; Hussian, Z.; Shen, Z. -X.; Crommie, M. F. Characterization of Collective Ground States in Single-Layer $NbSe_2$. *Nat. Phys.* **2016**, 12, 92.

(19) Wang, H.; Huang, X.; Lin, J.; Cui, J.; Chen, Y.; Zhu, C.; Liu, F.; Zeng, Q.; Zhou, J.; Yu, P.; Wang, X.; He, H.; Tsang, S. H.; Gao, W.; Suenaga, K.; Ma, F.; Yang, C.; Lu, L.; Yu, T. Tao, E. H. T.; Liu, G.; *et al.* High-Quality Monolayer Superconductor $NbSe_2$ Grown by Chemical Vapour Deposition. *Nat. Commun.* **2017**, 8, 394.

(20) Eknapakul, T.; King, P. D. C.; Asakawa, M.; Buaphet, P.; He, R. -H.; Mo, S. -K.; Takagi, H.; Shen, K. M.; Baumberger, F.; Sasagawa, T.; Jungthawan, S.; Meevasana, W. Electronic Structure of a Quasi-Freestanding $MoS_2$ Monolayer. *Nano Lett.* **2014**, 14, 1312.

(21) Zhu, H.; Wang, Y.; Xiao, J.; Liu, M.; Xiong, S.; Wong, Z. J.; Ye, Z.; Ye, Y.; Yin, X.; Zhang, X. Observation of Piezoelectricity in Free-Standing Monolayer $MoS_2$. *Nat. Nanotechnol.* **2015**, 10, 151.

(22) Ryu, H.; Chen, Y.; Kim, H.; Tsai, H. Z.; Tang, S.; Jiang, J.; Liou, F.; Kahn, S.; Jia, C.; Omrani, A. A.; Shim, J. H.; Hussian, Z.; Shen, Z. X.; Kim, K.; Min, B. I.; Hwang, C.; Crommie, M. F.; Mo, S. -K. Persistent Charge-Density-Wave Order in Single-Layer $TaSe_2$. *Nano Lett.* **2018**, 18, 689.

(23) Lin, M. K.; Hlevyack, J. A.; Chen, P.; Liu, R. Y.; Mo, S. -K.; Chiang, T. -C. Charge Instability in Single-Layer $TiTe_2$ Mediated by van-der-Waals Bonding to Substrates. *Phys. Rev. Lett.* **2020**, 125, 176405.

(24) Zhang, C.; Chuu, C. P.; Ren, X.; Li, M. Y.; Li, L. J.; Jin, C.; Chou, M. Y.; Shih, C. K. Interlayer Coupling Moiré Patterns, and 2D Electronic Superlattices in $MoS_2/WSe_2$ Hetero-Bilayers. *Sci. Adv.* **2017**, 3, e1601459.

(25) Reshak, A. H.; Auluck, S. Electronic and Optical Properties of the 1*T* Phases of $TiS_2$, $TiSe_2$, and $TiTe_2$. *Phys. Rev. B* **2003**, 68, 245113.

(26) Kresse, G.; Furthmüller, J. Efficient Iterative Schemes for *ab Initio* Total-Energy Calculations using a Plane-Wave Basis Set. *Phys. Rev. B* **1996**, 54, 11169.

(27) Kresse, G.; Furthmüller, J. Efficiency of *ab Initio* Total Energy Calculations for Metals and Semiconductors using a Plane-Wave Basis Set. *Comput. Mater. Sci.* **1996**, 6, 15.

(28) Kresse, G.; Joubert, D. From Ultrasoft Pseudopotentials to the Projector Augmented-Wave Method. *Phys. Rev. B* **1999**, 59, 1758.

(29) Perdew, J. P.; Burke, K.; Ernzerhof, M. Generalized Gradient Approximation Made Simple. *Phys. Rev. Lett.* **1996**, 77, 3865.

(30) Klmeš, J.; Bowler, D. R.; Michaelides, A. Chemical Accuracy for the van der Waals Density Functional. *J. Phys.: Cond. Matt.* **2010**, 22, 022201.

(31) Klimeš, J.; Bowler, D. R.; Michaelides, A., Van der Waals Density Functionals Applied to Solids. *Phys. Rev. B* **2011**, 83, 195131.

Figure 1. Atomic structures. (a) Unit cells of bulk $TiTe_2$ and $TiSe_2$ and a top view of the $TiTe_2/TiSe_2$ bilayer with the moiré superlattice unit cell indicated by a rhombus. The regions marked by red, blue, and maroon circles are locations near AA, AB, and AB' stacking configurations, respectively. (b) Detailed top and side views of the three stacking configurations. The vertical spacing $c$ is from energy minimization with the $TiTe_2$ and $TiSe_2$ layers constrained at the average in-plane lattice constant. (c) Comparison of the two-dimensional Brillouin zones of $TiTe_2$ and $TiSe_2$ monolayers and the $TiTe_2/TiSe_2$ moiré superlattice, with the last amplified by a factor of ten. The length of $\overline{\Gamma M}$ is 1.026, 0.960, and 0.064 $Å^{-1}$ for $TiSe_2$, $TiTe_2$, and the moiré bilayer, respectively.

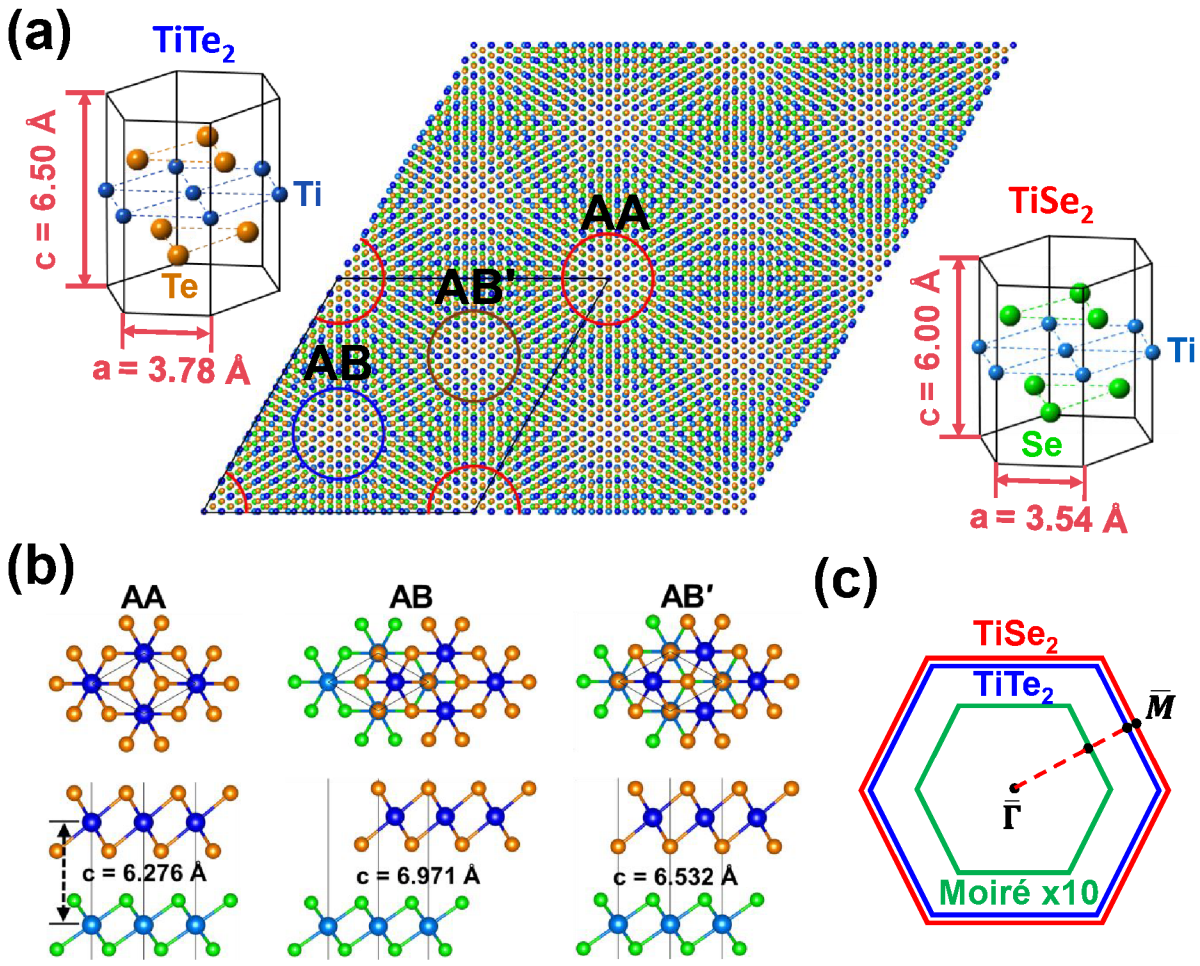

Figure 2. RHEED analysis. (a) A RHEED pattern taken from a bilayer-graphene-terminated 6*H*-SiC(0001). The horizontal direction corresponds to $\overline{\Gamma M}$. (b) A RHEED pattern taken from a $TiSe_2$ monolayer grown on the bilayer-graphene-terminated 6*H*-SiC(0001). (c) A RHEED pattern after further growth of a $TiTe_2$ monolayer on top of the $TiSe_2$ monolayer. (d) Line profiles for the RHEED patterns obtained by vertical integration over the red rectangular area displayed in (a). (e) Amplified views of the first-order peaks from the $TiTe_2/TiSe_2$ bilayer and fits in terms of a major contribution from the top $TiTe_2$ monolayer and a minor contribution from the bottom $TiSe_2$ monolayer. The intensity ratio of the minor component to the major component is 0.28.

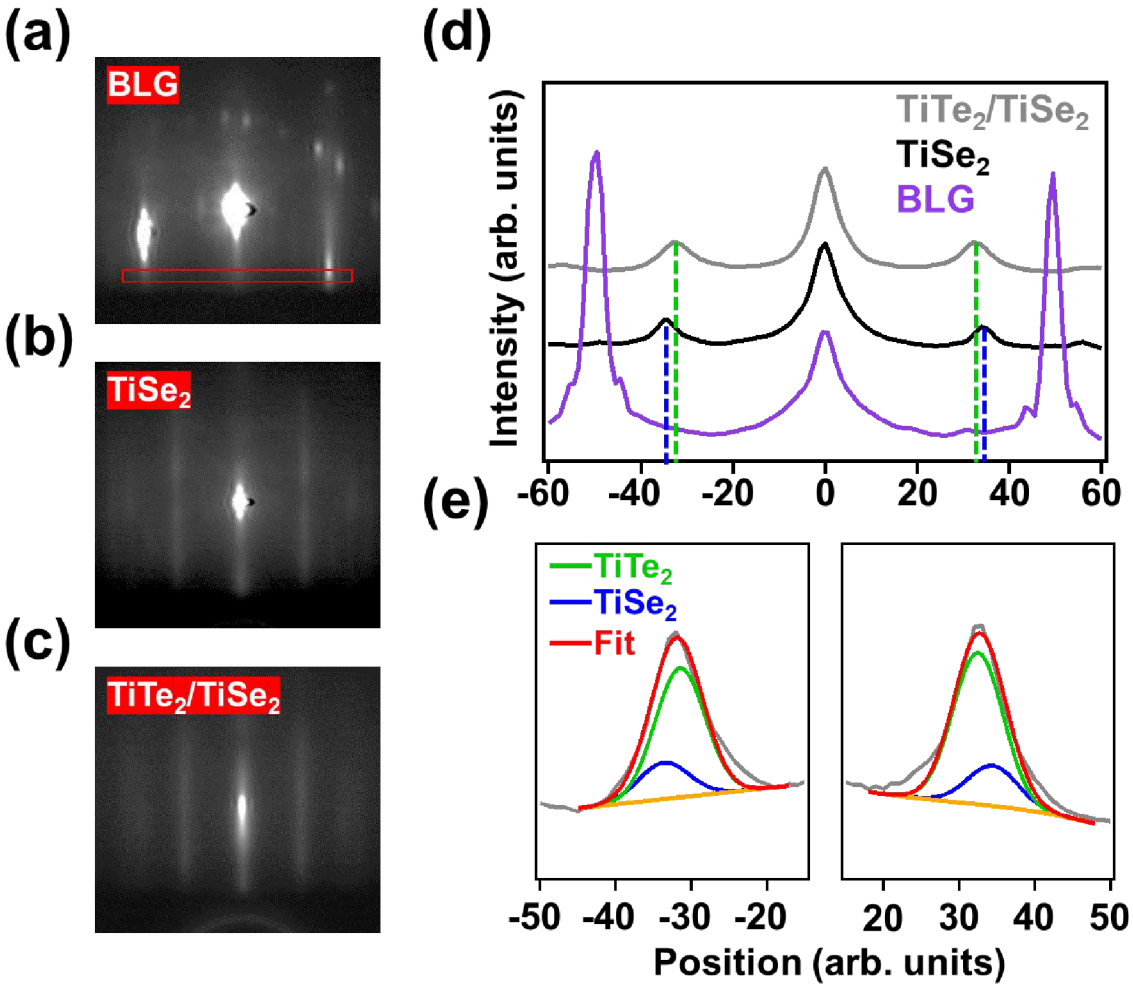

Figure 3. ARPES maps and theoretical band structures. (a) ARPES maps for monolayer $TiSe_2$, bilayer $TiTe_2/TiSe_2$, and monolayer $TiTe_2$ along $\overline{M}-\overline{\Gamma}-\overline{M}$ at 300 K. Composite band features C1-C4 are indicated. (b) Corresponding second-derivative maps overlaid with the computed band structures for monolayer $TiSe_2$ (blue curves) and $TiTe_2$ (red curves). (c) Same as (a) but with the sample at 20 K. Folded bands caused by (2x2) CDW formation in $TiSe_2$ and $TiTe_2$ monolayers are indicated. (d) Corresponding second-derivative maps overlaid with the computed band structures for monolayer $TiSe_2$ (blue curves) and $TiTe_2$ (red curves).

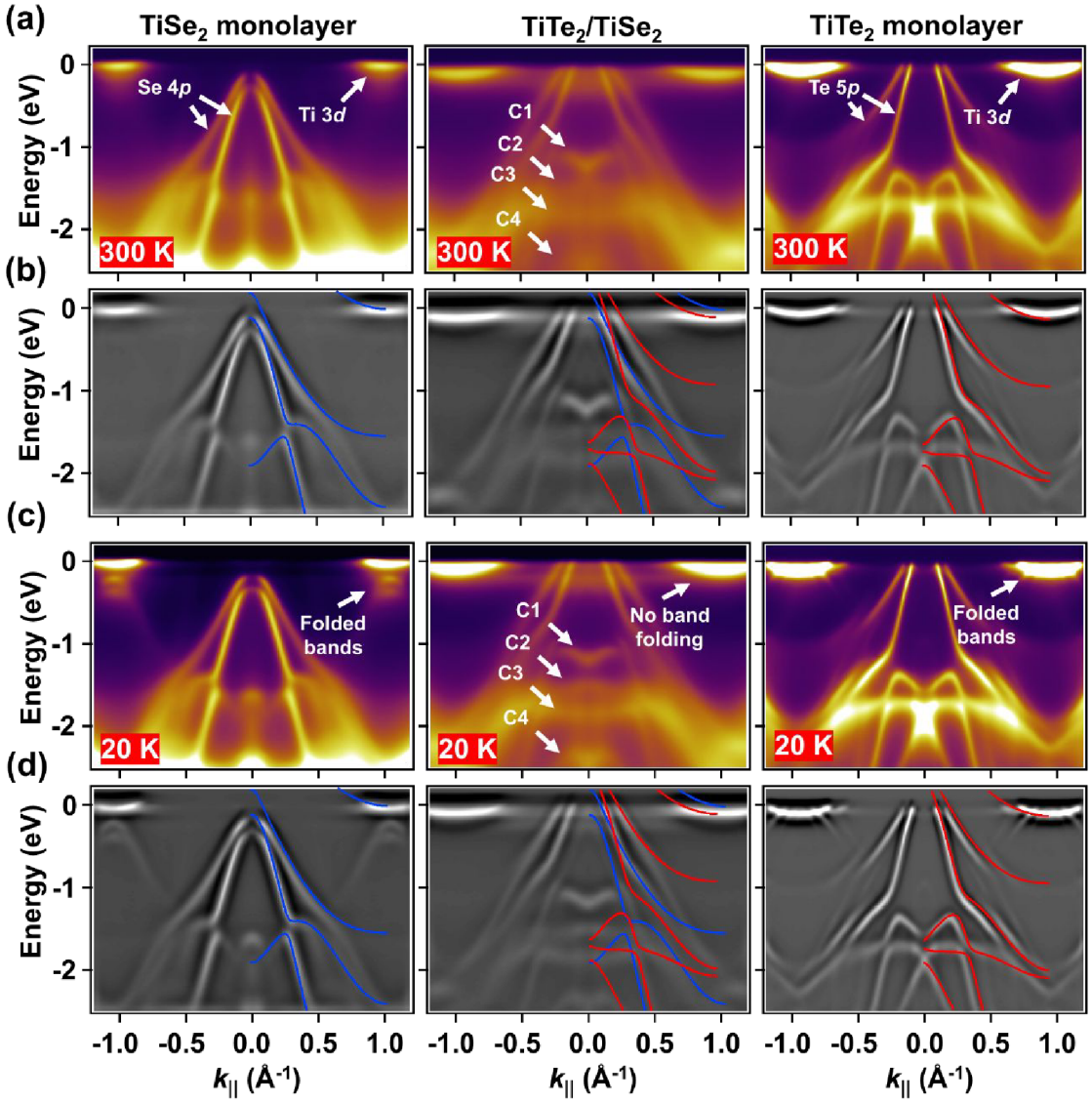

Figure 4. Comparison of experimental and theoretical band structures for the $TiTe_2/TiSe_2$ bilayer. (a) Calculated band structure with the orange and green colors indicating the $TiTe_2$ and $TiSe_2$ contributions, respectively. (b) Calculated spectral function with the intensity representing the contribution from the top $TiTe_2$ monolayer. (c) ARPES map at 20 K, reproduced from Figure 3. The white dots are the computed band structure with the dot size representing the $TiTe_2$ contribution. (d) Second-derivative ARPES map reproduced from Figure 3 but with the intensity scale over a portion of the data adjusted to highlight the composite bands C1-C4.